

## Spatial measure of reaction size in proton scattering

Makoto Ito<sup>1,2,a</sup>, Masataka Iwasaki<sup>1</sup>, Reiji Otani<sup>1</sup>, and Masashi Tomita<sup>1</sup>

<sup>1</sup>Department of Pure and Applied Physics, Kansai University, Yamatecho, 3-3-35, Suita, Japan

<sup>2</sup>Research center for Nuclear Physics (RCNP), Osaka University, Mihogaoka 10-1, Suita 567-0047, Japan

**Abstract.** The microscopic coupled-channel (MCC) calculations for proton +  $^{12}\text{C}$  inelastic scattering are performed in the energy range of  $E_p = 29.95$  MeV to 65 MeV. The nuclear interactions for the proton -  $^{12}\text{C}$  system are constructed from the folding model, which employs the internal wave function of  $^{12}\text{C}$ , obtained from the  $3\alpha$  resonating group method ( $3\alpha$  RGM), and an effective nucleon-nucleon interaction of the density-dependent Michigan three-range Yukawa (DDM3Y). The MCC calculation with the  $3\alpha$  RGM + DDM3Y nicely reproduces all of the differential cross sections for elastic and inelastic scattering in the angular range of  $\theta_{c.m.} = 30^\circ$  to  $120^\circ$ . We introduce a scattering radius, which characterizes a spatial size of the scattering area, from partial wave decompositions of an angle-integrated cross section. The scattering radii for the elastic scattering and the various inelastic channels, which involve the rotational or vibrational excitations and the  $3\alpha$  excitations in  $^{12}\text{C}$ , are derived. We found that the scattering radii for the inelastic channels with a well developed  $3\alpha$  structure are strongly enhanced in comparison to the scattering radii for the elastic and collective channels. This enhancement of the scattering radius for the  $3\alpha$  channel strongly suggests that the scattering radius is sensitive to a size of the intrinsic structure of the finally excited state in the scattering process.

## 1 Introduction

Clustering phenomena, in which a nucleus is decomposed into some subunits, are well known to appear in the excited states of the lighter mass system [1]. In  $^{12}\text{C}$ , for instance, three  $\alpha$  particles are weakly coupled in the excited  $0_2^+$  state, called Hoyle state, at  $E_x = 7.65$  MeV [2, 3], while they are strongly overlapped to each other in its ground  $0_1^+$  state. One of characteristic features in cluster states is an extension of a matter radius. Previous theoretical calculations suggest that a radius of a cluster state is larger by about 50% than a radius of a ground state [1–3].

Unfortunately, a size of a cluster state is difficult to measure directly by experiments because a cluster state has a very short life-time. In a naive expectation, however, such a spatial extension may be reflected in observables of scattering phenomena. In recent studies, there are several attempts to get the sign of a spatial extension of a cluster structure, especially in the reactions exciting the  $3\alpha$  state in  $^{12}\text{C}$  [4, 5]. In Ref. [5], for instance, a diffraction radius of the Hoyle state in  $^{12}\text{C}$  is speculated from the diffraction pattern observed in the differential cross section in the high energy proton scattering. In fact, a sign of an enhanced radius is confirmed for the Hoyle state of  $^{12}\text{C}$ .

<sup>a</sup>e-mail: itomk@kansai-u.ac.jp

Recently, we have proposed the method of the scattering radius on the basis of a partial wave decomposition of a coupled-channel problem [6]. The scattering radius is considered to characterize a spatial size of the reaction area for exclusive reactions. We can always derive the scattering radius just by doing the partial wave analysis of a scattering cross section. For the first time this method has been applied to a simple two channel problem in the proton ( $p$ ) +  $^{12}\text{C}$  scattering going to the Hoyle state [6], where the prominent enhancement of the scattering radius in the Hoyle channel has been confirmed.

In this report, the method of the scattering radius is extended to the multi-channel problem in the  $p$  +  $^{12}\text{C}$  scattering, going to the various inelastic channels that contain the collective excitations of the  $2_1^+$  and  $3_1^-$  states and the  $3\alpha$  excitations of the  $0_2^+$  and  $2_2^+$  states [7]. In the recent studies on  $^{12}\text{C}$ , the revised structure calculation has been performed, and the matter radius of the  $3\alpha$  states has been re-investigated [3]. According to the results, the matter radius of the  $2_2^+$  state is predicted to be strongly enhanced because the  $2_2^+$  state corresponds to the rotational excited states of the Hoyle  $0_2^+$  state [3]. Thus, the scattering radius for the  $2_2^+$  state is especially interesting in connection to the enhanced matter radius of this state. We analyze the scattering radii for various exit channels in connection to the respective excited states of the  $^{12}\text{C}$  nucleus.

There is another reason why we focus on the  $p$  +  $^{12}\text{C}$  scattering. Nucleon scattering from carbon is very important in the fields of nuclear engineering [8] and medical technology [9]. There are several coupled-channel (CC) calculations of the  $p$  +  $^{12}\text{C}$  inelastic scattering at the energy of  $E_p \leq 65$  MeV [10–12]. However, in these CC calculations, the nuclear potentials are treated in a phenomenological manner, and there is no approach of the full microscopic coupled-channels calculation, in which the nuclear interactions are calculated from a microscopic wave function of  $^{12}\text{C}$  based on the nucleon degrees of freedom and a reliable nucleon-nucleon (NN) interaction.

In our coupled-channel calculations, which is called the microscopic coupled-channel (MCC) calculation [6, 7, 13, 14], the nuclear interactions of  $p$  +  $^{12}\text{C}$  are constructed in the full microscopic manner, the folding model. In MCC, we use the internal wave function of  $^{12}\text{C}$  calculated from the  $3\alpha$  resonating group method (RGM) [2], while the density-dependent version of the Michigan 3 range Yukawa (DDM3Y) interaction [15–17] are employed for the effective NN interaction. The DDM3Y interaction was derived not in a phenomenological manner but from the microscopic calculation of infinite nuclear matter [17]. The microscopic interactions with  $3\alpha$  RGM + DDM3Y constitute the MCC calculation and hence, the MCC improves the shortcomings of the previous CC calculations, in which the phenomenological interactions are used. We apply the MCC calculation to the  $p$  +  $^{12}\text{C}$  inelastic scattering in the range of  $E_p = 29.95$  MeV to 65 MeV and check the reproducibility of the differential cross section. From the MCC calculation, we derive the scattering radii for the various exit channels and analyze their property in connection to the intrinsic structure of the  $^{12}\text{C}$  nucleus.

## 2 Theoretical framework

### 2.1 Coupled-channel equations

We solve a set of the coupled channel (CC) equations for the proton- $^{12}\text{C}$  system, which is given in the symbolic form

$$\left[ T_f(\mathbf{R}) + V_{f,f}(\mathbf{R}) - E_f \right] \chi_f(\mathbf{R}) = - \sum_{i \neq f} V_{f,i}(\mathbf{R}) \chi_i(\mathbf{R}). \quad (1)$$

Here, the subscripts  $f$  and  $i$  design a channel.  $T_f(\mathbf{R})$  represents the kinetic energy of the relative motion of the  $p$  +  $^{12}\text{C}$  system with a relative coordinate  $\mathbf{R}$ , while  $V_{f,i}(\mathbf{R})$  denotes the coupling potential for the transition from channel  $i$  to channel  $f$ .  $E_f$  represents the total energy in channel  $f$ , which is

given by the relation of  $E_f = E - \epsilon_f$  with a proton's incident energy  $E$  and an internal energy of  $^{12}\text{C}$ ,  $\epsilon_f$ .  $\chi_f(\mathbf{R})$  is the proton- $^{12}\text{C}$  relative wave function for channel  $f$ , which should be solved in the CC equation. In the present calculation, we include all discrete-excited states of  $^{12}\text{C}$  in addition to its ground  $0_1^+$  state: the rotational state of  $2_1^+$  (4.44 MeV), the vibrational  $3_1^-$  state (9.64 MeV), the  $3\alpha$  cluster states of  $0_2^+$  (7.65 MeV), and  $2_2^+$  (10.3 MeV).

In the pragmatic CC calculation, partial wave expansion with the channel-spin representation is applied to the total wave function, and the radial part of the relative wave function, such as  $\chi_{(sS_a)IL}^J(R)$ , is solved [13]. Here, the radial part of the relative wave function is classified in terms of the proton spin  $\mathbf{s}$ , the internal spin of  $^{12}\text{C}$ ,  $\mathbf{S}_a$ , the channel spin  $\mathbf{I} (= \mathbf{s} + \mathbf{S}_a)$ , the relative spin  $\mathbf{L}$ , and the total spin  $\mathbf{J} (= \mathbf{I} + \mathbf{L})$ . Here the subscript of  $a$  represents a suffix used to distinguish the internal state of  $^{12}\text{C}$  with the same spin ( $S_a = 0_1^+, 0_2^+$ , and so on). A set of the quantum numbers of  $(sS_a)I$  is a channel, while that of  $(sS_a)ILJ$  is usually called the sub-channel. In the present calculation, the proton spin is treated as the spin-less particle and hence, the sub-channel representation is reduced to  $(sS_a)ILJ$  ( $s = 0$  and  $S_a = I$ )  $\rightarrow S_aLJ$ . The CC equation is solved on the basis of the  $S_aLJ$  representation.

## 2.2 Nuclear coupling potential

The coupling potential ( $V_{f,i}(\mathbf{R})$ ) has a component of the nuclear ( $N$ ) and Coulomb ( $C$ ) parts, such as

$$V_{f,i}(\mathbf{R}) = V_{f,i}^{(N)}(\mathbf{R}) + V_{f,i}^{(C)}(\mathbf{R}) . \quad (2)$$

The nuclear potential is composed of the real ( $V_{f,i}(\mathbf{R})$ ) and phenomenological imaginary potentials ( $-iU_f(R)$ ),

$$V_{f,i}^{(N)}(\mathbf{R}) = \tilde{V}_{f,i}(\mathbf{R}) - iU_f(R) \cdot \delta_{f,i} . \quad (3)$$

The real part of the nuclear potential ( $\tilde{V}_{f,i}(\mathbf{R})$ ) is calculated by the folding model [13, 15, 16] which is expressed symbolically as

$$\tilde{V}_{f,i}(\mathbf{R}) = \int \rho_{f,i}(\mathbf{r}) v_{NN}^{DDM3Y}(|\mathbf{r} - \mathbf{R}|) d\mathbf{r} , \quad (4)$$

where  $\mathbf{r}$  denotes the coordinate measured from the center of the mass in the  $^{12}\text{C}$  nucleus. Here,  $\rho_{f,i}(\mathbf{r})$  represents the diagonal ( $f = i$ ) or transition ( $f \neq i$ ) densities of  $^{12}\text{C}$ , which is calculated by the resonating group method (RGM) [2] of the  $3\alpha$  cluster model. In Eq. (4),  $v_{NN}$  represents the effective nucleon-nucleon ( $NN$ ) interaction, which acts between a nucleon contained in  $^{12}\text{C}$  and an incident proton. The Coulomb interaction in Eq. (2) is calculated by assuming the uniform charge potential with a radius of  $R_C = 1.2A^{1/3}$  (fm), and no Coulomb coupling is included in the off-diagonal transition.

In the present work, the density-dependent Michigan three-range Yukawa (DDM3Y) is used for the effective  $NN$  interaction [15]. The explicit form of the DDM3Y interaction is given by

$$v_{NN}^{DDM3Y}(s) = \gamma \left( 1 + \alpha e^{-\beta\rho(s)} \right) v_{NN}^{M3Y}(s) , \quad (5)$$

with the M3Y interaction of

$$v_{NN}^{M3Y}(s) = \frac{7999}{4} \frac{e^{-4s}}{4s} - \frac{2134}{2.5} \frac{e^{-2.5s}}{2.5s} - J_0 \delta(s) . \quad (6)$$

In Eq. (5), the parameters of  $\alpha, \beta$  and  $\gamma$  depend on incident energy per nucleon [15]. Eq. (6) corresponds to the  $NN$  interaction for the spin ( $S$ ) and isospin ( $T$ ) singlet channel ( $S = T = 0$ ). Thus, there is no contribution from the long-range attractive potential generated by the one-pion exchanges.

The third term simulates the single-nucleon knock-on exchange with the energy-independent strength of  $J_0 = -262 \text{ MeV fm}^3$  [16]. In the present CC calculation, no modification is done for the folding potentials although a normalization factor is often introduced in the folding potential for the nucleus-nucleus scattering [18, 19].

The second term in Eq. (3) represents the imaginary potential, which is included only in the diagonal transition ( $f = i$ ). The imaginary potential is composed of two parts, such as

$$U_f(R) = W_{Vf}(R) + W_{Sf}(R) . \quad (7)$$

Here,  $W_{Vf}(R)$  and  $W_{Sf}(R)$  are the Woods-Saxon (WS) potentials with volume-type and surface-type form factors, respectively. Three parameters, such as strength ( $W_{0f}$ ), radius ( $R_f$ ), and diffuseness ( $a_f$ ), are included in each of the WS potentials. These six parameters are channel dependent, and they are optimized so as to reproduce the observed differential cross sections as much as possible. In the present calculation, we neglect the imaginary potentials in the off-diagonal transition for simplicity. All the parameters used in the present MCC calculation are listed in Ref. [7]

### 2.3 Definition of the scattering radius

In Eq. (1), the coupling problem among the sub-channels, such as  $S_a L J \rightarrow S'_a L' J$  is solved. The angle-integrated cross section can be decomposed into the partial wave ( or sub-channel ) component,  $\sigma(LL'S_a)$ , which is designed by the initial orbital spin  $L$ , the final spin of a target  $S_a$ , and the final orbital spin  $L'$  for the scattering two particles. Since the initial state of the  $^{12}\text{C}$  target is in the spin-less state ( $S_a = 0^+$ ), the initial orbital spin  $L$  is equal to the total spin  $J$  ( $L = J$ ).

In order to characterize a size of scattering area to produce the final channel, we simply define the effective orbital spin  $\tilde{L}$  [6] for the final spin state of ( $S_a$ ) from the partial cross section  $\sigma(LL'S_a)$  like

$$\tilde{L}(S_a) = \sqrt{\frac{\sum_{LL'} \tilde{L}^4 \sigma(LL'S_a)}{\sum_{LL'} \tilde{L}^2 \sigma(LL'S_a)}} \quad (8)$$

with  $\tilde{L} = \sqrt{L(L+1)}$  which is calculated from the initial orbital spin  $L$ . The effective orbital spin is obtained by the fourth and second powers of the magnitude of the orbital spin,  $\tilde{L} = \sqrt{L(L+1)}$ . In Eq.(8), we simply assume the same functional form as the root-mean-squared radius for the matter density distribution [6]. The scattering radius  $R_{SC}$  corresponding to  $\tilde{L}$  can be simply obtained from the relation of  $\tilde{L} = kR_{SC}$ , where  $k$  denotes the wave number of the incident channel, measured in the laboratory system.

The magnitude of  $R_{SC}$  depends on the definition of  $\tilde{L}$  in Eq. (8), and there are other possibilities to define the effective orbital spin. The variation of  $\tilde{L}$  has been discussed in Ref. [6], and we have pointed out that the definition of Eq. (8) gives a reasonable size for the elastic scattering, which is comparable to the matter radius of the ground state of  $^{12}\text{C}$ . Thus, in the present analysis, we also use Eq. (8) for the definition of the effective orbital spin  $\tilde{L}$  although other possibilities of the functional form should be considered for  $\tilde{L}$ . Other possibility in the definition of  $\tilde{L}$  will be discussed in a forthcoming article.

## 3 Results

### 3.1 Differential cross sections

We show the results of the full MCC calculation with the nuclear interaction in Eqs. (3) and (4). The left and right panels in figure 1 show the results of the differential cross sections of the elastic ( $0^+$ )

and  $0_2^+$  channels, respectively [7]. The comparison of the CC calculations (solid curves) with the experiments (asterisks) is done in the energy range of  $E_p = 29.95$  MeV to 65 MeV.

The CC calculation for the elastic ( $0_1^+$ ) channels nicely reproduces the overall features of the observed differential cross sections except for the backward angles of  $\theta_{c.m.} \geq 120^\circ$  at the energies of  $E_p \leq 39.95$  MeV. In the MCC calculation, a prominent valley appears at the angle of  $\theta_{c.m.} = 130^\circ$ , and the calculated cross section quickly increased beyond  $130^\circ$  in comparison to the experimental data. We have also calculated the differential cross section of the inelastic scattering to the  $2_1^+$  and  $3_1^-$

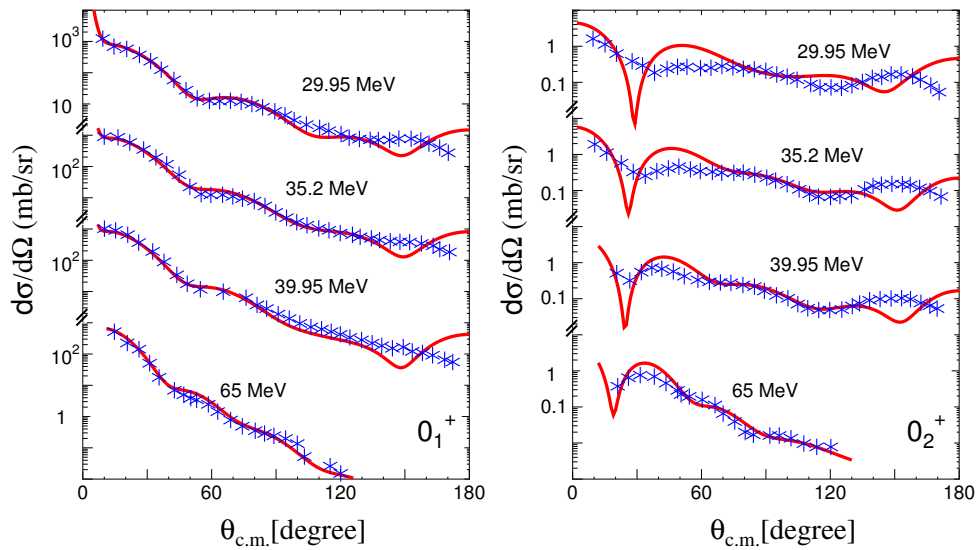


**Figure 1.** Left panel: Differential cross section of the elastic ( $0_1^+$ ) scattering in the range of  $E_{lab} = 29.95$  MeV to 65 MeV. The asterisks and the curves represent the experimental data and the theoretical calculations, respectively. Right panel: Same as the left panel except for the inelastic  $0_2^+$  channel. These figures are taken from Ref. [7].

states, which are the member of the rotational and vibrational excited states from the ground state, respectively, in the same energy range [7]. In these two channels, the angular distributions are nicely reproduced up to  $\theta_{c.m.} \leq 130^\circ$  although the calculation for the  $3_1^-$  channel considerably underestimates the experimental cross section at the forward angular range of  $\theta_{c.m.} \leq 30^\circ$ . The valley-peak structures confirmed in the CC calculation for the  $0_1^+$  channel are also observed in the these two channels, and the CC calculation is out of phase around  $\theta_{c.m.} = 130^\circ$ . Therefore, a failure at the backward scattering beyond  $\theta_{c.m.} = 130^\circ$ , which is the out of phase in the valley-peak structure, is common in all of the collective channels, such as  $0_1^+$ ,  $2_1^+$ , and  $3_1^-$ .

The valley-peak structures at the backward angles of  $\theta_{c.m.} = 130^\circ$  were also observed in the previous CC calculation based on the soft-rotator model [10]. The theoretical picture of  $^{12}\text{C}$  in our calculation, which is based on the composite system of the  $3\alpha$  particles, is very different from the approach in Ref. [10], which employs the one-body-like collective motion of  $^{12}\text{C}$ . However, the shortcomings in calculating the angular distribution seem to be common in these two models.

The results of the CC calculation for the  $0_2^+$  state, which has the well-developed  $3\alpha$  structures, are shown in the right panel in Fig. 1 [7]. In all the energy ranges, the theoretical calculations reasonably reproduce the global features of the observed cross sections. However, the deviations of the CC

calculation from the experimental data are more prominent in comparison to the  $0_1^+$  channels. At the backward angles of  $\theta_{c.m.} \sim 150^\circ$  the CC calculation is out of phase in comparison to the experimental data. This out of phase is the same feature as the collective channels. Moreover, a sharp valley appears in the CC calculation at the angle of  $\theta_{c.m.} = 30^\circ$ , and this valley is deviated from the observed data except for the incident energy of  $E_p = 65$  MeV.

The channel coupling effect on the  $0_2^+$  channel is analyzed [7]. The direct coupling of  $0_1^+ \rightarrow 0_2^+$  is quite weak because the intrinsic structures are very different with each other. However, the coupling of the  $0_2^+$  and  $2_2^+$  channels is very strong because the  $2_2^+$  state corresponds to the rotational state of the  $0_2^+$  state [2, 3], which is a weakly coupled state of the  $3\alpha$  particles. Therefore, the angular distribution of the  $0_2^+$  channel is strongly affected by the coupling to the  $2_2^+$  channel [7, 14].

The present CC calculations are quite successful in reproducing the differential cross sections of all the final channels in the angular range of  $\theta_{c.m.} = 30^\circ \sim 120^\circ$  although the fit to the experimental data depends considerably on the exit channels. There is a common feature in the deviation between the theory and the experiment: the out of phase structure at the backward angle of  $\theta_{c.m.} \geq 130^\circ$ . However, the overall feature of the angular distributions is reasonably reproduced in the whole angular range.

### 3.2 Partial cross sections and scattering radii at $E_p = 65$ MeV

From the CC calculation in Fig. 2, we can obtain the partial cross section, which is explained in Sec. 2.3. In Fig.2, we show the distributions of the partial cross section  $\sigma(L)$  for the spin-less channels of the  $0_1^+$  (asterisks) and  $0_2^+$  (squares) at  $E_p = 65$  MeV. In the case of the spin-less final state, the partial cross section in Eq. (8) is labeled by the incident orbital spin  $L$  (or total spin  $J$ ) because of  $S_a = 0$  and  $L = L' = J$ . In Fig. 2, only the nuclear part of the partial cross sections is plotted, and the Coulomb part is subtracted in the elastic  $0_1^+$  channel. The magnitude of the partial cross sections is normalized by their total summation of  $\sigma_{tot.} = \sum_L \sigma(L)$ , such as  $\sigma(L)/\sigma_{tot.}$ .

In the partial cross sections of these two exit channels, we can observe the different shape: the single peak structure in the elastic channel (asterisks) and the double peaks structure in the  $3\alpha$  channel (solid squares). This double peak structure is originated from the feature of the monopole coupling potential of  $0_1^+ \rightarrow 0_2^+$ . The monopole coupling potential changes its sign at a certain  $p-^{12}\text{C}$  distance and hence, the coupling potential has the one node in the spatial distribution. This nodal behavior is because of the condition of the volume (or nucleon number) conservation. Thus, the double peak structure is considered to mainly reflect the distribution of the coupling potential, while the distribution of the elastic scattering is determined from the diagonal potential in the elastic  $p+^{12}\text{C}_{g.s.}$  channel.

In this figure, moreover, we can clearly observe the partial cross section of the  $0_2^+$  channel has more extended distribution than that of the elastic channel. The peak position in the elastic channel exists around  $L = 3$ , while the higher peak in the  $0_2^+$  channel locates at  $L = 5$ . This extension strongly

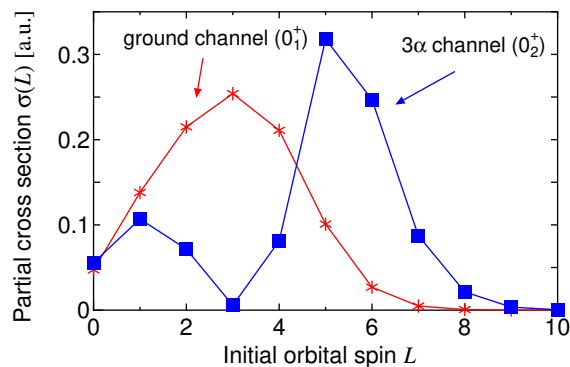


**Figure 2.** Distribution of the partial cross sections at  $E_{lab}=65$  MeV. The abscissa and the ordinate show the initial orbital spin  $L$  and the respective partial cross section  $\sigma(L)$ , respectively. Both of the partial cross sections are normalized by the total cross section,  $\sigma_{tot.} = \sum_L \sigma(L)$ .

suggests that a size of the scattering area to produce the  $0_2^+$  channel is larger than that for the spatial area where the elastic scattering occurs.

A characteristic distributions of the partial cross sections can be observed in other inelastic channels. The normalized partial cross sections for the  $2_1^+$  and  $2_2^+$  channels, which correspond to the rotational excited channels of the  $0_1^+$  and  $0_2^+$  channels, respectively, are shown in Fig. 3. Here the definition of  $\sigma(L)$  is  $\sigma(L) \equiv \sum_{L'} \sigma(LL'S_a) / \sigma_{tot.}$  and  $\sigma_{tot.} = \sum_{LL'} \sigma(LL'S_a)$ . Both of the distributions have a single peak structure, and the peak position of the  $2_2^+$  channel locates at  $L = 6$ , which is shifted to the high  $L$  side in comparison to the peak position of the  $2_1^+$  channel ( $L = 4$ ). The distribution of the partial cross sections for the  $3_1^-$  channel also spreads in the higher  $L$  region with a peak at  $L = 5$ . although its distribution is not shown in the figure.

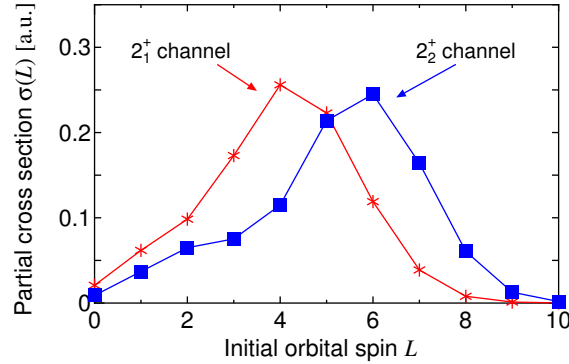


**Figure 3.** Same as Fig. 3 except for the  $2_1^+$  (asterisks) and  $2_2^+$  (squares) channels.

The partial cross sections in Figs. 2 and 3 suggest that the spatial size of the reaction area depends on the final channel. In order to characterize the spatial size of each reaction channel more clearly, the effective orbital spins  $\bar{L}$  and the scattering radii,  $R_{sc}$  are calculated according to the definition of Eq. (8). The obtained effective orbital spins  $\bar{L}$  and the scattering radii  $R_{sc}$ , are summarized in table 1. In this table, the matter radii ( root mean squared radii,  $\bar{r}$  ) of all the states [2] are also shown in the bottom row for comparison.

	$0_1^+$	$0_2^+$	$2_1^+$	$2_2^+$	$3_1^-$
$\bar{L}$	4.6	6.4	5.7	6.8	6.0
$R_{sc}$ [fm]	2.6	3.6	3.2	3.9	3.4
$\bar{r}$ [fm]	2.4	3.5	2.4	4.0	2.8

**Table 1.** Effective orbital spin  $\bar{L}$  and the scattering radius  $R_{sc}$  at  $E_{lab}=65$  MeV. The matter radius  $\bar{r}$  of the  $0_1^+$ ,  $0_2^+$ ,  $2_1^+$ ,  $2_2^+$  and  $3_1^-$  states are also shown in the bottom column [2].  $R_{sc}$  and  $\bar{r}$  are shown in units of fm.

From table 1, we can see the enhancement of  $R_{sc}$  for the inelastic scattering going to the  $0_2^+$ ,  $2_2^+$  and  $3_1^-$  states, which are the resonance states just above the  $3\alpha$  threshold, in comparison to the scattering radius of the  $0_1^+$  and  $2_1^+$  states. The enhancement of the scattering radii in the  $0_2^+$  and  $2_2^+$  channels can be attributed to the spatial extension of the  $3\alpha$  structures of these states.

On the contrary, there is a considerable enhancement of the scattering radius in the  $3_1^-$  channel ( $R_{sc} = 3.4$  fm), which is comparable to the scattering radius of the  $0_2^+$  state ( $R_{sc} = 3.5$  fm), although this state does not have the  $3\alpha$ -cluster structure but the spatially compact structure [1, 2]. The  $3_1^-$  state is a resonant state existing above the  $3\alpha$  threshold of  $E_{3\alpha}=7.27$  MeV ( $E_x=9.6$  MeV). Therefore, the  $3_1^-$  state has an extended tail in its radial wave function. This extension is considered to be one of the origins for the enhanced scattering radius of the  $3_1^-$  state.

In particular, the  $R_{SC}$  of the  $2_2^+$  is strongly enhanced, and this enhancement is originated from the peak shift to the higher  $L$  region in the respective partial cross section, as shown in Fig. 3. The  $2_2^+$  state is the  $3\alpha$  rotational state, which has much more extended matter radius, and this large radius has recently been pointed out by Funaki et al. [3]. The scattering radius does not necessarily mean the matter radius of a target nucleus itself but our scattering radius is consistent with the matter radius of the  $2_2^+$  state. Thus, the scattering radius derived from the partial cross section can be used for the measure of the spatial size, which reflects the intrinsic structure of the final channel.

### 3.3 Energy systematics of the scattering radii

Finally, we discuss the incident energy dependence of the scattering radii  $R_{SC}$ , which is shown in Fig. 4. The results in Fig. 4 represent that the scattering radius does not depend so much on the incident energy. Therefore, the qualitative features of the scattering radius are almost invariant with respect to the variation of the incident energy. In all the energy range considered here, the scattering radius of the  $2_2^+$  state (triangles) is the largest of all the channels, while the enhancements are commonly observed in the  $0_2^+$  (squares) and  $3_1^-$  (open circles) channels. In contrast to these enhanced channels, the scattering radii of the ground  $0_1^+$  (asterisk) and its rotational state of  $2_1^+$  (solid circles) are clearly suppressed. The magnitude correlation in the scattering radii observed in Fig. 4 is consistent with the matter radii predicted in the  $3\alpha$  cluster model shown in table 1 although the order of  $0_2^+$  and  $3_1^-$  is inverted only at  $E_{lab}=29.95$  MeV.

The scattering radii shown in Fig. 4 contain the errors, which arise from the theoretical ambiguity of the potential parameters. As shown in Fig. 1, the reproduction of the angular distributions is restricted in the angular range of  $30^\circ \leq \theta_{c.m.} \leq 120^\circ$ , and a simultaneous reproduction over all the channels is a little difficult in a common parameter set of the imaginary potential and the strength of the folding potential. The scattering radii basically depend on the potential parameters which are determined from fitting the theoretical calculation to the experimental data.

In order to estimate the ambiguity of the scattering radii, which is caused by the several choice of the parameter sets (or the reproducibility of the experimental angular distributions), we have searched for the several parameter sets of the potential, which can reproduce each of exit channels separately. For example, one parameter set is optimized for the reproduction of the elastic channel, while the other parameter sets can reproduce only the Hoyle  $0_2^+$  channel, and so on.

From the searched potential parameter sets, we can determine the various scattering radii, and the standard deviations from the averaged radii are evaluated as the errors contained in the theoretical calculation. The resultant magnitude of the error reaches about  $\pm 10\%$ , at most, in all the exit channels although this error bars may be slightly changed in the future parameter search. Thus, the qualitative

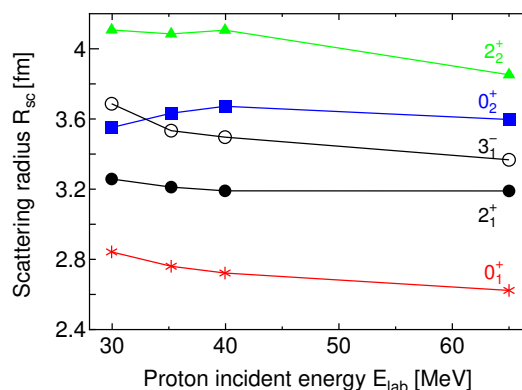


**Figure 4.** The incident dependence of the scattering radius. Asterisks, solid circles, open circles, solid squares and solid triangles are the results of the  $0_1^+$ ,  $2_1^+$ ,  $3_1^-$ ,  $0_2^+$  and  $2_2^+$  channels, respectively.

features of the scattering radius are invariant even if much more tuned potentials in comparison to the present calculation are employed in the CC calculation.

## 4 Summary and discussion

We have performed the microscopic coupled-channel (MCC) calculation in the proton +  $^{12}\text{C}$  scattering in the energy range of  $E_p = 29.95$  MeV to 65 MeV. In the framework of MCC, the real part of the nuclear potentials is derived from the precise wave function of  $^{12}\text{C}$ , which is calculated by the  $3\alpha$  resonating group method ( $3\alpha$  RGM), and the reliable nucleon-nucleon (NN) interaction, such as the Density-Dependent Michigan 3-range Yukawa (DDM3Y). In addition to the real potential, we have introduced an imaginary potential with the form factor of the Woods-Saxon potential for the diagonal coupling, and the parameters in the imaginary potentials are optimized to reproduce the differential cross sections.

The MCC calculation with  $3\alpha$  RGM + DDM3Y can nicely reproduce the observed angular distributions in the angular region of  $\theta_{c.m.} = 30^\circ$  to  $120^\circ$ . The fit to the experimental data in the present MCC calculation is superior to the previous coupled-channel calculations that were based on the phenomenological treatment in the coupling potential [10–12]. Reproduction of the experiments by the microscopically derived nuclear interactions is an important development in the theoretical calculations. However, the reproduction of the detailed structures is still insufficient especially in the backward ( $\theta_{c.m.} \geq 120^\circ$ ) and forward scattering ( $\theta_{c.m.} \leq 30^\circ$ ). In the backward scattering, the theoretical calculations for all the exit channels commonly generate the valley-peak structures, which are out of phase in the oscillating pattern of the angular distribution by comparing with the experimental data. Since the proton scattered to the backward angle strongly feels the interior density of the  $^{12}\text{C}$  target, the modification to the interior part of the transition density may be important for the improvement of the fit to the backward scattering.

We have also defined the effective orbital spin  $\bar{L}$  from the partial wave components of the angle-integrated differential cross sections. The scattering radius, which is derived from  $\bar{L}$ , is considered to correspond to the spatial size of the reaction area, which produces the final state in the exclusive reaction. In principle, the scattering radius can always be defined when the partial wave analysis is possible for the differential cross section. In a recent study, effective radii in the deuteron induced reaction are derived from the continuum-discretized coupled-channel, and radii for the inclusive reactions are clearly defined [20]. In contrast to this approach, the present method is useful for the definition of the radius in an exclusive reaction, going to a specific channel.

The method of the scattering radius has been applied to the present MCC calculation for the  $p + ^{12}\text{C}$  scattering, and the scattering radii of the elastic and inelastic scattering to  $0_2^+$ ,  $2_1^+$ ,  $2_2^+$  and  $3_1^-$  states have been derived. We have found a clear enhancement of the scattering radius for the final inelastic channels in comparison to the elastic channel. In particular, we confirmed the enhanced scattering radius in the  $3\alpha$  cluster channels ( $0_2^+$  and  $2_2^+$ ). This enhanced scattering radius for the cluster channels is attributed to the spatial extension of the  $3\alpha$  structure.

It is very important to clarify the relation between the scattering radii and the respective matter radii, especially in the inelastic scattering to the Hoyle  $0_2^+$  state. In Refs. [21, 22], the sensitivity of the differential cross section to the size of the final state is discussed in the inelastic scattering of  $\alpha + ^{12}\text{C} \rightarrow \alpha + ^{12}\text{C}(0_2^+)$ . According to the analysis, the oscillating pattern of the differential cross section is insensitive to the size of the  $0_2^+$  state [21], and the oscillation is mainly determined from the size of the transition potential of  $0_1^+ \rightarrow 0_2^+$  [22]. The authors concluded that the oscillation pattern in the differential cross section does not reflect a size of the final  $3\alpha$  structure itself.

The partial cross section of the  $0_1^+ \rightarrow 0_2^+$  in the present analysis reveals the double peak structure, and these double peaks are originated from the nodal behavior of the monopole transition [6], in

which the transition potential changes the sign at a certain  $p - {}^{12}\text{C}$  distance. Thus, the global shape of the partial cross section is dominated by the transition potential, and this result is consistent with the results of Refs. [21, 22]. However, there is the possibility that the higher partial wave part in the partial cross section beyond the second peak is sensitive to the size of the final state. The sensitivity of the partial cross section to the size of the diagonal potential of the final  $0_2^+$  state must be carefully checked in future studies.

In the present coupled-channel calculation, we have treated only the  $p + {}^{12}\text{C}$  scattering system. The systematic studies are also important to establish the validity of the method of the scattering radius. For example, the analysis of the  $\alpha$  and  ${}^3\text{He}$  scatterings by  ${}^{12}\text{C}$  is important because the previous studies have discussed the evolution of the Airy structures in the angular distribution in connection to the enhanced radius of the Hoyle state [18, 19]. Furthermore, the  ${}^{16}\text{O}$  nucleus is another typical example of the cluster structure. In this nucleus, the  $\alpha + {}^{12}\text{C}$  [23, 24] and  $4\alpha$  [24] structures appear in the excited states. In particular, a recent study in Ref. [24] suggests that the  $0_6^+$  state corresponds to the  $4\alpha$  dilute state, and it is expected to have the extended matter radius. Thus, the analysis of the inelastic scattering of proton and  $\alpha$  particle by the  ${}^{16}\text{O}$  nucleus is very interesting. Systematic studies are now underway.

## References

- [1] K. Ikeda et al., Prog. Theor. Phys. **68**, 1 (1980), and references therein.
- [2] Y. Fukushima and M. Kamimura, Proceedings of the International Conference Nuclear Structure, J. Phys. Soc. Jpn. **44**, 225 (1977); M. Kamimura, Nucl. Phys. A **351**, 456 (1981).
- [3] Y. Funaki et al., Phys. Rev. C **67**, 051306(R) (2003), and references therein.
- [4] A. N. Danilov et al., Phys. Rev. C **80**, 054603 (2009).
- [5] K. Iida, S. Koide, A. Kohama, K. Oyamatsu, Mod. Phys. Lett. A **27**, 1250020 (2012).
- [6] M. Tomita, M. Iwasaki, R. Otani, and M. Ito, Phys. Rev. C **89**, 034619 (2014).
- [7] M. Tomita, M. Iwasaki, R. Otani, K. Horio, and M. Ito, Phys. Rev. C **92**, 024609 (2015).
- [8] M. B. Chadwick, P. G. Young et al. Nucl. Sci. and Eng. **131**, 293 (1999).
- [9] M. B. Chadwick, P. M. DeLcua, Jr and R. C. Haight, Rad. Protect. Dos. Vol. **70**, 1 (1997).
- [10] Efrem Sh. Sukhovitskii et al., Phys. A **640** 147 (1998).
- [11] S. Kato et al., Phys. Rev. C **31** 1616 (1985).
- [12] T. Nojiri and M. Kamimura and M. Sano, Prog. Theor. Phys. **66**, 1906 (1981).
- [13] M Ito, Y. Hirabayashi, and Y. Sakuragi, Phys. Rev. C **66**, 034307 (2002); M. Ito, Y. Sakuragi, and Y. Hirabayashi, Phys. Rev. C **63** 064303(2001).
- [14] M. Ito, Y. Sakuragi, and Y. Hirabayashi, Eur. Phys. Jour. A **5**, 373 (1999).
- [15] M. E. Brandan, G. R. Sarchler, Phys. Rep. **285**, 143 (1997).
- [16] G. R. Satchler and W. G. Love, Phys. Rep. **55**, 183 (1979).
- [17] G. Bertsch, J. Borysowicz, H. Macmanus and W. G. Love, Nucl. Phys. A **284**, 399 (1977).
- [18] S. Ohkubo and Y. Hirabayashi, Phys. Rev. C **70**, 041602 (2004).
- [19] Sh. Hamada et al., Phys. Rev. C **87**, 024311 (2013).
- [20] S. Hashimoto et al., Phys. Rev. C **83**, 054617 (2011).
- [21] M. Takashina and Y. Sakuragi, Phys. Rev. C **74**, 054606 (2006).
- [22] M. Takashina, Phys. Rev. C **78**, 014602 (2008).
- [23] Y. Suzuki, Prog. Theor. Phys. **55**, 1751 (1976); *ibid*, Prog. Theor. Phys. **56**, 111 (1976).
- [24] Y. Funaki et al., Phys. Rev. Lett. **101**, 082502 (2008).